

# Concept and Demonstration of a Low-cost Compact Electron Microscope Enabled by a Photothermionic Carbon Nanotube Cathode

Casimir Kuzyk, Alexander Dimitrakopoulos, Alireza Nojeh\*

Department of Electrical and Computer Engineering, The University of British Columbia, Vancouver BC, V6T 1Z4, Canada

Quantum Matter Institute, The University of British Columbia, Vancouver BC, V6T 1Z4, Canada

\*Corresponding author: [alireza.nojeh@ubc.ca](mailto:alireza.nojeh@ubc.ca)

The scanning electron microscope (SEM) delivers high resolution, high depth of focus and an image quality as if microscopic objects are seen by the naked eye. This makes it not only a powerful scientific instrument, but a tool inherently applicable to nearly all fields of study and curiosity involving the small scale. However, SEMs have remained complex, expensive, and beyond the reach of many. To broaden access, we demonstrate an SEM using simple, low-cost, off-the-shelf components, and hobby-level electromechanics; this has been enabled by a unique thermionic electron source based on a carbon nanotube array excited by low optical power<sup>1</sup>. The instrument offers sub-micrometer resolution, a depth of focus of several hundred micrometers, and an image quality comparable to commercial SEMs; it also tolerates poor vacuum and moist specimens, making it broadly applicable. It has a flexible design that lends itself to easy customization for different use scenarios. We provide the conceptual approach and high-level design in this paper; the detailed blueprints of our specific implementation will be provided separately online. We hope that specialists and non-specialists alike will build variations that fit their own needs and interests, helping electron microscopy expand into diverse new sectors of society and industry.

## I. Introduction

In 1966, the head of a living flour beetle graced the cover of the San Francisco Chronicle—an example of early microscopic images allowing the public a glimpse into previously unseen intricacies of the small scale<sup>2,3</sup>. Such visuals were obtained with the scanning electron microscope (SEM), taking advantage of its high resolution and depth of focus combined with a natural “lighting” quality. These features combine to produce visuals as if the specimen is seen by the naked eye, but with great magnification. As such, not only has the SEM been a workhorse of high-resolution imaging in industry and academia, but few scientific instruments, aside from the light microscope, have captivated society's imagination as deeply as the SEM. However, unlike light microscopy, which has become increasingly accessible—an extreme example is the \$1 US “Foldscope”<sup>4</sup>—electron microscopy remains inflexible, expensive, and inaccessible to both the public and many professionals. Even those with access to commercial instruments typically have to adapt to the SEM by preparing a specimen for *ex-situ* imaging in a shared facility, which precludes a wide range of possible experiments. It would be beneficial if a broader part of society—including researchers, grade-school students<sup>5</sup>, healthcare providers in remote regions, ecologists, mining engineers, air and water quality monitoring experts, and artists—had the power of the SEM at their fingertips.

Shortly after the development of charged-particle optics and the first transmission and scanning electron microscopes in the 1920s-1940s, as early as in the 1950s pioneers such as DeLong and Oatley (the “father of the modern SEM”<sup>6</sup>) envisioned the utility of simpler and lower-performance but more

accessible instruments<sup>7-9</sup>. The challenge of enabling broad access to electron microscopy has been undertaken in various forms since. Table-top instruments are now available from established manufacturers and new players, such as the ThermoFisher Scientific Phenom, the DeLong Instruments LVEM 5, and the Voxa Mochii<sup>TM</sup> to name a few, but these instruments typically cost over ~\$50,000 US (and commonly over \$100,000 US). Project NanoMi, led by the National Research Council Canada, introduces a promising open source electron microscope design<sup>10-15</sup>. Miniaturized instruments have also been proposed and relevant components developed to various degrees<sup>16-30</sup> (for example for testing within a commercial SEM using its electron beam), including in the context of electron-beam lithography and multibeam applications<sup>31-41</sup>. The development of microfabricated components has also seen significant recent advances as part of a systematic effort at Wrocław University of Science and Technology to create miniature electron microscopes and other devices<sup>42-44</sup>. An alternative path to accessibility is for skilled enthusiasts to build their own SEM. However, the SEM, as known today, is a complex machine, and it is rare for an individual to undertake the challenge of building one—a notable example is presented on the YouTube channel “Applied Science”<sup>45</sup>. A different approach, avoiding specialized skills and expensive components, may help open this path broadly.

In this paper, we present an approach to developing a new type of SEM that is simple and does not rely on specialized designs and components or domain expertise, and demonstrate that it opens a broad and useful region in the performance-cost-flexibility space.

This paper is about the concept and the high-level design and outcomes. The detailed design of the specific prototype that we have developed, including mechanical structure, electronic circuits, codes, and components list, will be provided separately online. We emphasize that the concept presented here does not rely on a particular embodiment. Our prototype is only one example, and variations of the instrument can be made using different designs to suit specific application scenarios; the form factor, exact components, control circuits, and software may vary as long as the overall concept remains consistent with what is described here.

## **II. Approach and results**

We present an SEM that uses low-cost, common components, and hobby-level prototyping and electronic skills to build. The flexible nature of the design allows easy customization for integration into other experimental setups or workflows, and even portability. This may help enable a new modality of SEM-user interaction where the SEM adapts to the user. A schematic outlining the main components of the prototype, along with a table summarizing its key features, is shown in figure 1. We note that the photos in the schematic are of the actual components used in the prototype, and emphasize their simplicity and low-cost nature; this will be discussed in more detail later. Images of various specimens obtained using backscattered electrons are also shown in the figure. The instrument’s large depth of focus and inherently intuitive image quality are seen—features that can be better appreciated in a direct imaging comparison with an advanced optical microscope (also in figure 1)—demonstrating the capability and usefulness of this SEM.

Also shown in figure 1 are images of a calibration grid and a tin-on-carbon specimen, showing the prototype’s resolution of a few hundred nanometers—we claim a conservative value of better than 1 micrometer. This is consistent with the instrument’s electron beam probe size of <310 nm as obtained

from point-projection imaging experiments, charged-particle optics simulations, and analytical calculations, as will be described later. This imaging performance level, while not competitive with conventional commercial SEMs, fills a gap that is relevant to a wide range of applications. For example, the effectiveness of SEMs with even relatively low magnification has been established for clinical applications<sup>46</sup>.

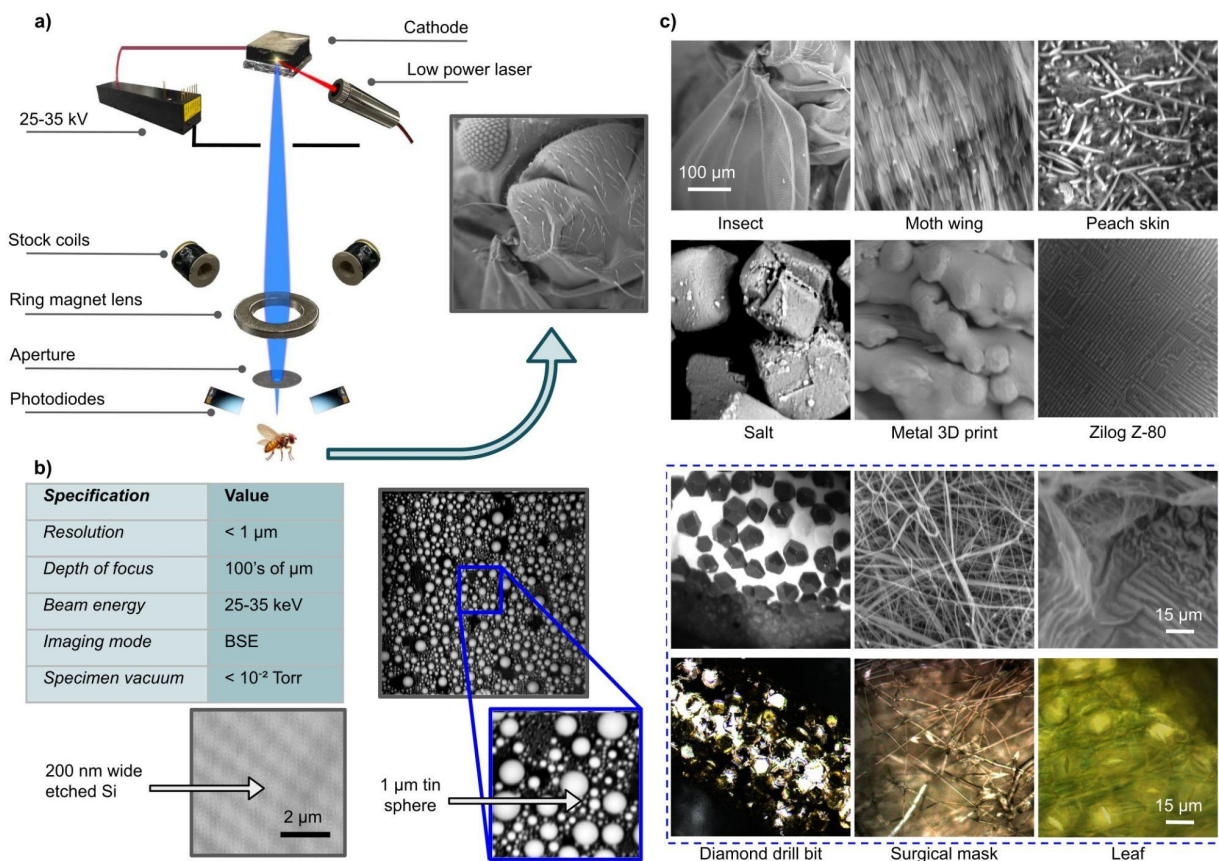


**Figure 1. Instrument concept and performance.** (a) Conceptual schematic of this SEM including actual photos of its key components, all of which are generic and not custom-built for this instrument, and an image of an insect head taken using our prototype. (b) Performance specifications of the instrument and images of two commercial calibration specimens (etched-lines-in-silicon and tin-spheres-on-carbon) revealing this SEM's sub-micrometer imaging resolution. (c) The top three rows include examples of images of diverse specimens obtained using this SEM, with an acceleration voltage between 25 and 35 kV (scale bars approximate). It is worth pointing out that beam stigmation was not used for obtaining these images. (The insect, moth wing, and surgical mask samples were metal-coated before imaging, whereas the others were not.) For comparison, the bottom row includes light microscope images of the same specimens as in the third row. The light microscope used was a high-quality, research-grade instrument (Olympus LEXT OLS3100), yet the complimentary, if not superior, imaging quality of this SEM prototype can be seen, notably its greater depth of focus.

In creating this SEM, our approach has been different from those of previous efforts, in that the instrument is designed around a unique electron source that enables a simplified overall system. This source uses a localized light-induced heating effect in an array of aligned carbon nanotubes (CNTs), also known as a CNT forest (see Supplementary Information for the growth process). We have previously reported this effect and described its properties<sup>47-51,1</sup>. Here we only briefly state the basic

phenomenon: A spot on a macroscopic CNT forest is illuminated by a focused beam of light. Due to effectively low thermal conduction loss<sup>52-54</sup>, the optically-generated heat remains localized to an area approximately the size of the incident light spot, leading to a strong temperature rise and thermal electron emission (more commonly known as thermionic emission). This can be achieved using only modest optical irradiance as readily available from a laser pointer, or even sunlight focused by a handheld lens. The incandescent glow of such a “Heat Trap” spot is depicted on the CNT forest at the top of the figure 1 schematic. This electron source combines several advantages of different conventional sources: tolerance of poor vacuum (more tolerant than conventional thermionic emitters); not requiring power electronics and thermal management (similar to field-emitters); optically-defined electron emission spot (similar to photo-emitters). The combination of these advantages allows one to greatly simplify the electron beam focusing optics, the structural design, and the pumping requirements. More detail about the electron source as relevant to this SEM is given in Methods. (Here we note that carbon nanotube-based field-emitters have been studied for various applications<sup>55</sup>, including incorporation into microcolumns and conventional electron microscopes<sup>56-59</sup>, and emphasize that our source is not a field-emitter, but an optically-excited thermionic emitter.)

### **III. Instrument design, build, and analysis**

A photo of the SEM prototype and cuts of the main sections of its electron-optical column are shown in figure 2. The CNT forest is excited by a small laser pointer and the emitted electrons are accelerated and travel down the column toward the specimen. Small electromagnets are used for raster-scanning the beam (as well as alignment and stigmation, if desired). A simple N52 neodymium ring magnet acts as the focusing lens, where coarse focusing is carried out by adjusting the position of the ring magnet along the column, and fine focusing is accomplished by tuning the acceleration voltage typically in the range of 25-35 keV. Backscattered electrons are detected using basic silicon pn-junction diodes (not specifically designed for high-energy electrons) facing the specimen. The specimen can be moved and repositioned as desired during live imaging at >5 frames/second simply by manually sliding the plate on which it resides—an experience similar to that of using an ordinary light microscope. The instrument is controlled by a basic microcontroller, which communicates with a graphical user interface written in Python on a laptop computer using a USB connection. The entire SEM was made using hobby-level machining experience and off-the-shelf components. CNT forests are also available commercially, costing a few hundred dollars—a price that can decrease significantly through bulk production.

The cost to build our prototype, not including the vacuum pump (more on that below), was ~\$5,000 US; this can be cut to almost half if the machining is carried out in-house and/or structural components are made using simpler and additive manufacturing techniques, as well as by using lower-cost alternatives to the high-voltage power supply and feedthrough. The design is discussed further in Methods and more detail on specimen flexibility in particular regarding moist specimens, pumpless operation, electron optics, noise and shielding, and safety aspects are given in Supplementary Information; example additional micrographs taken by the instrument are also provided in Supplementary Information.

It is worth mentioning that we made two SEM prototypes, which were identical in terms of the

electron-optical performance, demonstrating the repeatability of the design; the more recent prototype (shown in figure 2) incorporated the sample movement mechanism and updated electronics and system software to allow for live imaging.

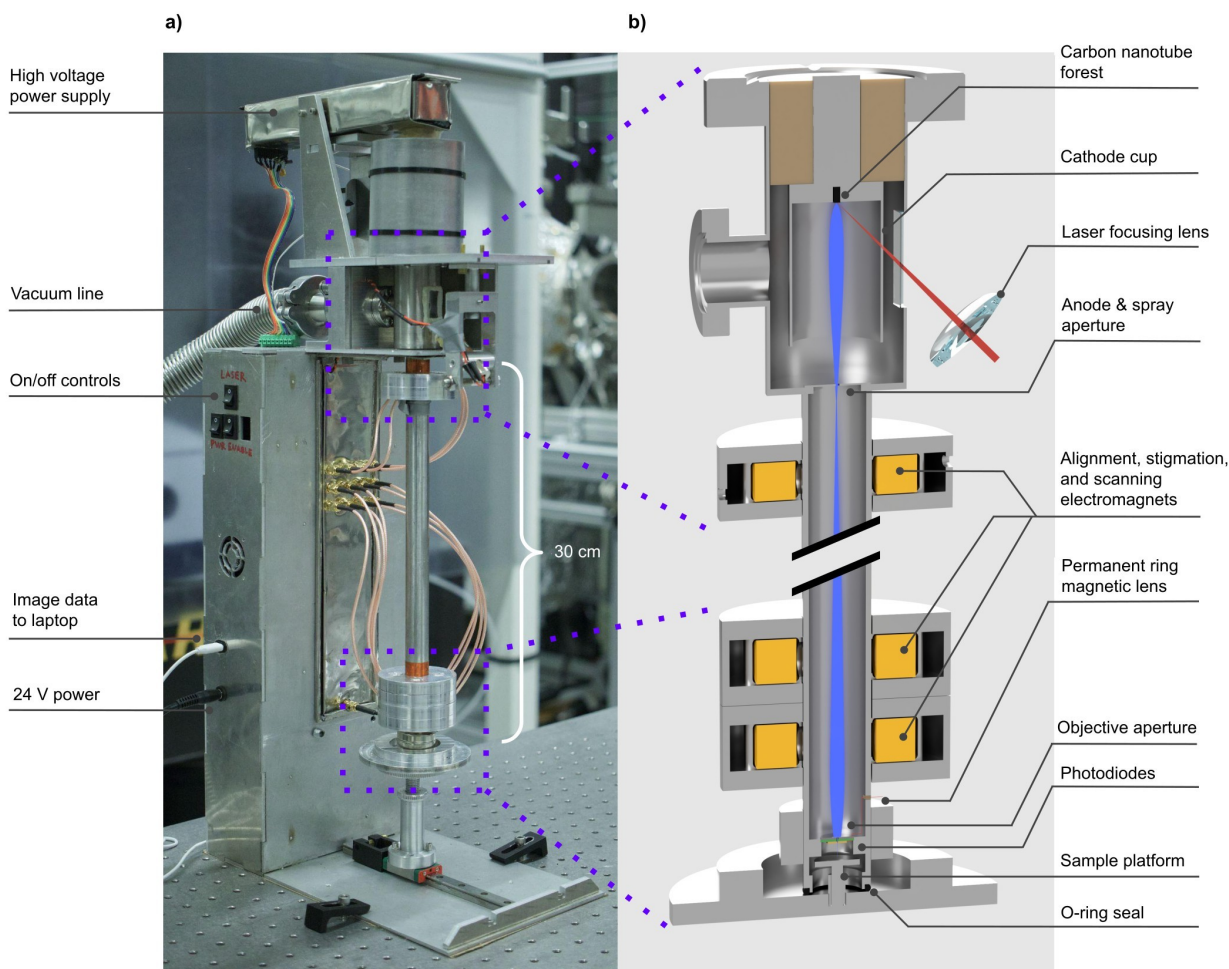


**Figure 2. Prototype photo and design.** (a) Photo of the instrument. Other than the electron-optical column, the rest of the microscope platform is only used to house the electronics and provide mechanical support, and can be replaced by any other desired design/configuration. (b) A computer-aided design (CAD) section view of the electron-optical column. The detailed description is given in Methods.

An overview of the electron-optical analysis of the column is presented in figure 3a. The electron emission spot is  $<40 \mu\text{m}$  in diameter (as defined by the focused laser spot on the CNT forest surface). The electrostatic field created by the negatively charged cathode cup has a focusing effect on the emitted beam to create a crossover spot with a diameter of  $<10 \mu\text{m}$  immediately following the anode aperture. This crossover is then demagnified 50-65 times by the objective lens (depending on the acceleration voltage value, which is typically in the range of 25-35 kV), which would yield an electron probe with a diameter of  $<200 \text{ nm}$  at the specimen in absence of aberrations. Chromatic and spherical aberration contributions to the probe size are calculated at 32 nm and 3 nm, respectively. Including all these effects, we estimate an overall probe diameter of  $<250 \text{ nm}$ . The crossover spot and probe diameter were also measured through point-projection microscopy experiments (figure 3b) to be  $6 \mu\text{m}$

and 310 nm, respectively. The details of the dimensions, simulations, calculations, and experiments are given in Methods. These calculated and measured electron probe diameters at the specimen are consistent with the prototype’s imaging resolution of better than 1 micrometer.

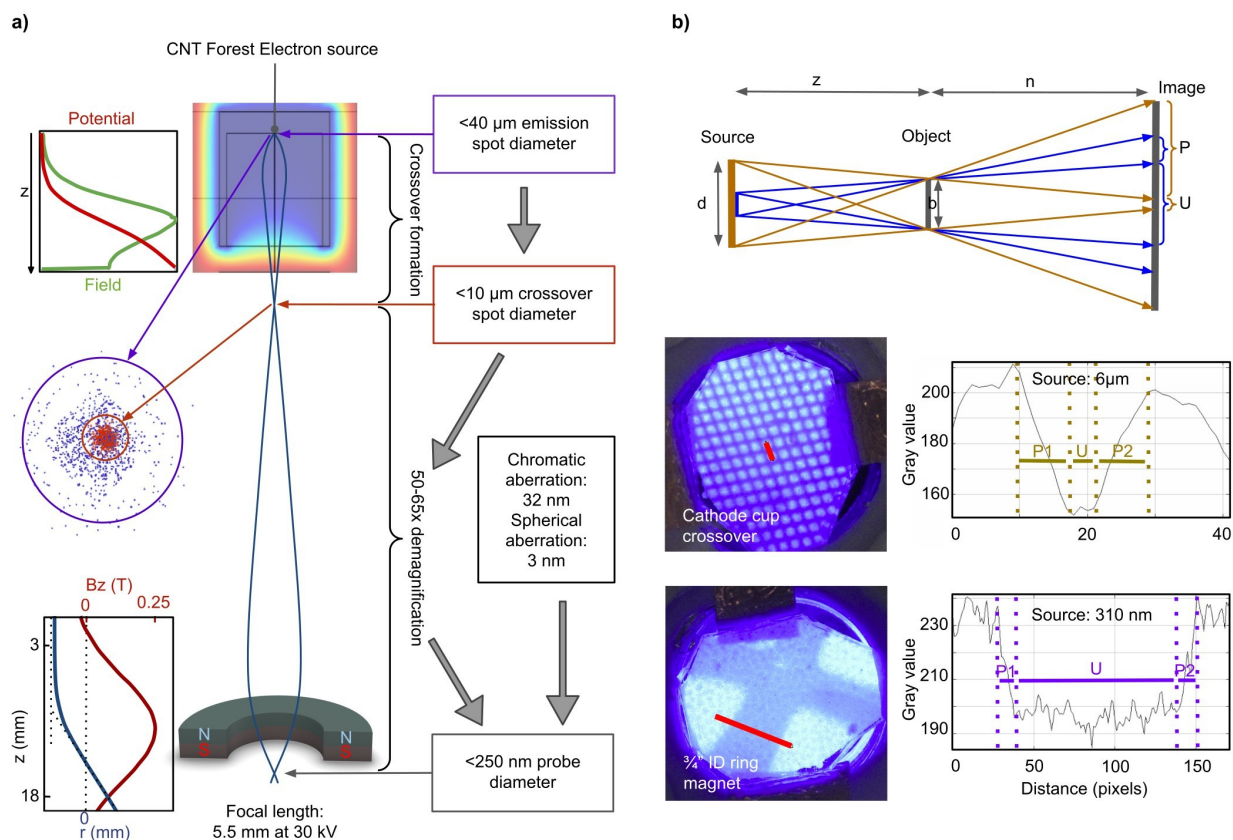


**Figure 3. Electron-optical analysis.** (a) Probe diameter analysis: starting from the electron emission spot diameter of  $<40\ \mu\text{m}$  from the CNT forest, charged-particle tracing simulations show the formation of a beam crossover with a diameter of  $<10\ \mu\text{m}$  shortly after the acceleration region (colour map shows the simulated potential distribution, and blue and red dots are beam particles at emission and crossover planes, respectively), which is then demagnified by the objective lens to  $<200\ \text{nm}$  as calculated using beam tracing within the measured magnetic field distribution (bottom plot) of the ring magnet. Given contributions from spherical and chromatic aberrations, the probe diameter is estimated to be  $<250\ \text{nm}$ . More details on the aberrations and ring magnet focal length calculations can be found in Methods. (b) Probe diameter measurement: (top row) schematic of the point-projection microscopy experiment—we used a metallic 2000 mesh as the object; (middle row) image on the phosphor screen and line profile of the image along the red line for the experiment where the beam crossover is used directly as the source; (bottom row) results for the case where the electron probe (beam crossover after focusing by the ring magnet) is used as the source. The crossover and probe diameters are thus obtained to be  $6\ \mu\text{m}$  and  $310\ \text{nm}$ , respectively. The details of these calculations and experiments are given in Methods.

#### IV. Vacuum considerations

While this SEM can be designed for mounting on an existing high-vacuum or ultra-high-vacuum chamber, those are not a requirement. In our imaging experiments, the specimen compartment was typically held at only  $\sim 1 \times 10^{-2}$  Torr. This tolerance to poor vacuum translates to the instrument’s suitability for various types of specimens, including moist and biological ones (Supplementary Information figures S1 and S2). For example, we were able to pick fresh tree leaves from outside our

laboratory and image them directly without dehydrating or metal coating, while experiencing negligible specimen charging (Supplementary Information figure S2). In fact, the specimen compartment does not have any special vacuum requirements, and can be made to operate at variable pressures and even at the level of environmental and wet SEM<sup>60-63</sup>.

Our electron source and column were typically held at  $\sim 1 \times 10^{-4}$  Torr using a vacuum pump, but in principle they do not need active pumping, and may instead be permanently sealed-off under vacuum, similar to a cathode ray tube device. This is particularly desirable for reducing cost and increasing portability (we have previously demonstrated vacuum-sealed glass vessels incorporating CNT forest electron sources<sup>49,64</sup>; other examples are sealed-off gyrotron and X-ray sources using carbon nanotube cathodes<sup>65,66</sup>). In this scheme, the electrons exit the column through an electron-transparent membrane and strike the specimen *in-situ*, be it in high vacuum, low vacuum, or even air. This concept has long been established in atmospheric electron microscopy<sup>67-70</sup>; even atomic scale imaging has been demonstrated at ambient pressure<sup>71</sup>. If the membrane thickness and subsequent travel distance in the specimen environment are within a few electron mean free paths, a useful portion of the beam will remain unscattered and preserve imaging resolution (while the scattered electrons only act to increase background noise). For example, after traversing a 20-nm-thick silicon nitride membrane and 50  $\mu\text{m}$  of atmospheric gas, about 1% of 15-keV electrons are estimated to remain unscattered and, at 0.1 atmosphere, the value rises to 10%; image enhancement methods have also proven effective in this context<sup>72,73</sup>. Below about 0.01 atmosphere, where environmental SEMs operate, scattering in air becomes practically negligible. As for scattering in the membrane, it can be reduced by using thinner membranes made from mechanically stronger materials. For example, bi-layer graphene is shown to improve contrast and signal-to-noise ratio by  $\sim 4$  and  $\sim 12$  times, respectively, compared to  $\sim 10$ - $20$ -nm-thick nitride<sup>74</sup>. We have also carried out preliminary demonstrations of pumpless, sealed-off operation, as well as imaging in rough vacuum ( $\sim 40$  Torr) using an electron-transparent silicon nitride membrane; the results are presented in Supplementary Information figure S3.

## V. Summary and outlook

The premise of this work has been to demonstrate a simple and inexpensive SEM constructed entirely using non-specialist parts and techniques. This instrument delivers images that are qualitatively similar to those of commercial SEMs, and complements or outperforms advanced optical microscopes, covering a wide range of presently unaddressed applications. It is thus a practically useful instrument that could enable broad access to electron-beam imaging in society and industry. Furthermore, it is possible to manufacture sealed-off, pumpless versions of this SEM using the technologies established for cathode ray tube television sets, including their high-voltage supply and control electronics. Large-scale production and distribution at a cost of less than a thousand dollars thus appears feasible, extending access widely. Taking a broader view than only imaging applications, one may speculate that the widespread availability of a simple ‘point-and-shoot’ electron beam device, which is the core of this instrument, may prove useful and enable new applications.

In future designs, multiple independent detectors may be placed around the objective aperture to cover different backscattering angular ranges, and their signals used for enhanced topographical imaging. In addition to backscattered electron detection, other established imaging modalities may be used,

including electron-beam-induced current and secondary electron detection using simple gaseous detectors<sup>61,63,75</sup>. Additional electron-optics may also be incorporated to provide magnification after the specimen for transmission-mode imaging. The addition of X-ray or cathodoluminescence detectors would also enable spectroscopy.

The images shown here were obtained using off-the-shelf neodymium ring magnets as the only focusing element. We present additional results using various such magnets, and discuss simple strategies such as the inclusion of an iron pole-piece or a condenser lens for improving the resolution to tens of nanometers, in Supplementary Information. However, there is much room for performance enhancement even without improving the hardware, through software-based filtering of known electrical and mechanical noise, and deconvolution of the point spread function of the electron probe<sup>76,77</sup>.

Similarly to other areas, artificial intelligence (AI) methods have found their way into electron microscopy and related techniques. Recent examples include resolution improvement in three-dimensional imaging<sup>78,79</sup>, automating image acquisition and segmentation<sup>80</sup> and crystal structure identification<sup>81</sup>, increasing access to atomic-scale dynamics in *in-situ* microscopy<sup>82</sup>, and automating experimental workflows<sup>83</sup>. The use of AI in microscopy is only expected to grow and, going forward, much progress may originate from innovation in software rather than hardware. The availability of vast image datasets from diverse application domains for both supervised and unsupervised training of AI systems will be crucial in this regard. Not only will the electron microscopy platform presented here benefit from AI-based resolution enhancement and related advances, but it is also intended to enable a wide range of users to contribute to diverse image datasets, in turn helping advance the use of AI in electron microscopy. Just as AI models have recently surprised all by their abilities to glean and synthesize information, they may similarly surprise us in their ability to construct physically legitimate high-resolution electron micrographs based on low-resolution hardware data. Placing SEMs in the hands of many may thus help accelerate the advancement of electron microscopy to make the small world accessible to all.

## METHODS

### **Optically excited thermionic electron source based on CNT forest**

As mentioned in the main text, we have previously reported that heat remains localized at the illuminated spot on a CNT forest<sup>47,1</sup>—we have characterized this heat localization in detail using both simulations and thermographic and hyperspectral temperature mapping experiments<sup>52,84</sup>. As a result, the thermionic electron emission spot is defined by the focused spot of the illuminating laser beam.

In the present SEM, the CNT forest is illuminated by an off-the-shelf laser pointer whose beam is collimated by its integrated optics, and then focused using a plano-convex lens with a focal length of 50 mm. The laser we used had a wavelength of 650 nm and was chosen for its low cost and small form factor. A power of a few tens of mW is sufficient for producing the necessary electron emission current, and the choice of wavelength is a matter of availability; we have experimentally demonstrated this thermionic emission effect with wavelengths ranging from 266 nm to 1064 nm<sup>48,50</sup>.

Typical values of emission current are in the range of 1-10  $\mu$ A and, with most of the electrons being

blocked by the objective aperture, the probe current reaching the specimen is estimated to be on the order of a nanoampere or less. The reduced brightness of the emitter was estimated at  $1.82 \times 10^4 \text{ Am}^{-2} \text{sr}^{-1} \text{V}^{-1}$  through experiments where the electrons emitted from the CNT forest were accelerated towards a phosphor screen directly facing it<sup>85</sup>. This is comparable to a typical thermionic tungsten emitter if operated at a similar temperature<sup>86</sup>. However, this value could be increased by an increase in laser power (and therefore temperature and emission current density) and a decrease in laser spot size.

### **Cathode assembly**

The electron source assembly consists of a CNT forest attached at the base of the cathode cup (a conductive cylinder similar to that discussed in [87]). Other than having a focusing effect on the electron beam to create a crossover point (figure 3 of the main text), the cup also acts to limit the local electric field near the CNT forest and prevent spurious field-emission. The cathode cup length, diameter, and distance to the anode were tuned using charged-particle simulations in COMSOL Multiphysics<sup>®</sup> to minimize the crossover spot diameter before experimental implementation. The CNT forest and cathode cup are biased at the negative acceleration voltage using a feedthrough directly connected to the output of a negative-polarity variable-voltage source (capable of up to 40 kV).

We verified in charged-particle simulations and experimentally that, even if the laser spot was not centered on the axis of the beam column, the electric field between the cathode cup and the anode would naturally center the electron beam. As such, alignment of the cathode cup to the beam column axis is more important than alignment of the actual emission spot. Our SEM prototype uses parts made in an undergraduate metal shop with tolerances greater than  $\pm 0.05$ ", which has been sufficient for mechanical alignment of the cathode cup to the beam column.

Based on knife-edge measurements (figure M1), we obtain a focused laser beam waist diameter of  $< 40 \mu\text{m}$ , with a workable depth of focus of a few millimeters. In the SEM, the laser is focused through a glass window on the cathode vacuum compartment and a small opening on the side of the cathode cup onto the CNT forest (figure 2 of the main text). The glass window is attached to the cathode compartment using low-vapour-pressure epoxy. The laser is held in place in a two-axis movable joint to facilitate its positioning on the CNT forest side surface. It should also be noted that the opening on the side of the cathode cup was simulated in COMSOL Multiphysics<sup>®</sup> to have a negligible impact on the electric field distribution inside the cup, and so does not affect the shape of the electron beam.

Due to the bulk nature of the CNT forest, and the ability to use an emission spot misaligned to the electron-optical axis, the focused optical spot position can be changed periodically. Thus, although the CNT forest sidewall may suffer degradation over time due to high-temperature operation, the lifetime of the emitter as a whole is a collective of all spots' independent lifetimes. We have used the same CNT forest source for 300+ hours of operation without any noticeable decrease in imaging performance.

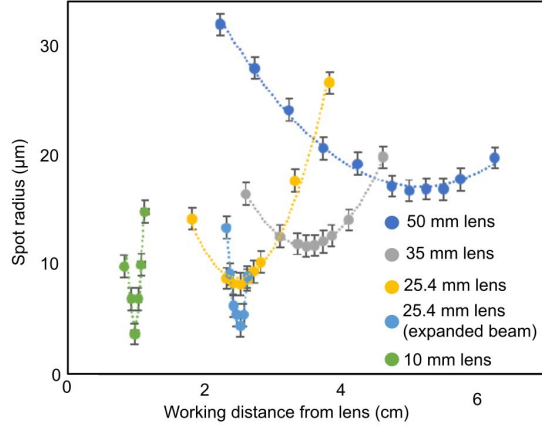


**Figure M1. Choice of optical lens.** a) Focused laser spot radius as a function of working distance for various lenses with different focal lengths; our SEM prototypes used the 50-mm lens, resulting in a focused laser spot radius of  $<20 \mu\text{m}$  (diameter of  $<40 \mu\text{m}$ ).

### Analysis of electron-optical demagnification, aberrations, and probe size

Electrons emitted from the cathode accelerate towards the anode. A significant portion of them pass through the 1-mm-diameter anode aperture and travel down the field-free column until the objective aperture, which truncates the beam prior to focusing. Focusing is accomplished by a permanent-magnet objective lens. The magnetic field distribution of this ring magnet was measured using a gaussmeter mounted on a translation stage, and fed to a simulation solving the paraxial ray equation, yielding a focal length of 4.6-6 mm for beam energies in the range of 25-35 keV (figure M2). Given the distance from the cathode cup crossover plane to the focal plane of the objective lens, the demagnification is 50-65 times. With an initial crossover spot diameter of  $<10 \mu\text{m}$  as described before, the probe size is thus  $<200 \text{ nm}$  if aberrations are neglected. Based on the diameter of the objective aperture and its distance to the focal plane, spherical aberration is obtained to be 3 nm using

$$(1) \quad d_{\text{sph}} = 0.5C_s\beta^3,$$

where  $d_{\text{sph}}$  is the spherical aberration,  $C_s$  is the spherical aberration coefficient, and  $\beta$  is the semi-angle of electron beam convergence. We have measured the energy spread of thermionic emission from the CNT forest to be  $<1 \text{ eV}^{88,89}$ , so the ripple of the power supply, which is  $9 \text{ V}_{\text{p-p}}$  at 30 kV, is the dominant source of chromatic aberration, which is obtained to be 32 nm using

$$(2) \quad d_{\text{chr}} = 2C_c(\Delta E/E_0)\beta,$$

where  $d_{\text{chr}}$  is the chromatic aberration,  $C_c$  is the chromatic aberration coefficient,  $\Delta E$  is the energy spread of the electron beam, and  $E_0$  is the acceleration voltage. We used the focal length of the objective lens as the values of  $C_c$  and  $C_s$ . Given the above demagnification analysis and aberration calculations, we expect the overall probe diameter to be  $<250 \text{ nm}$ .

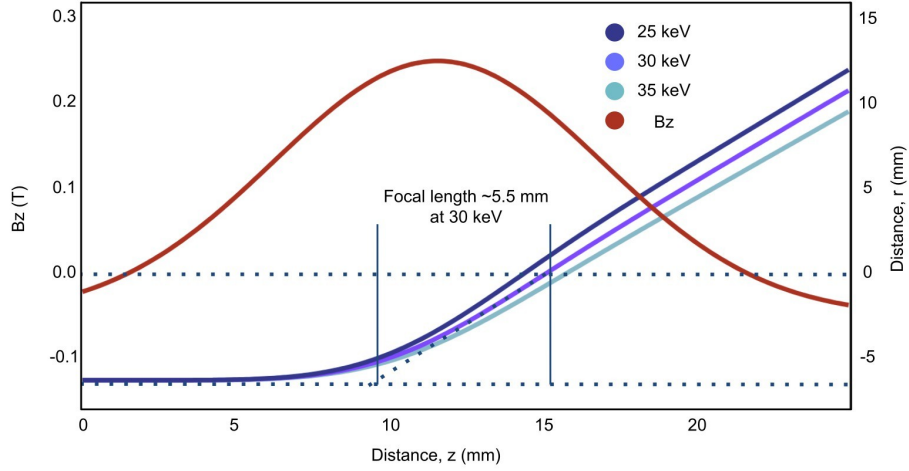


**Figure M2. Electron beam focusing using permanent magnet objective lens.** On-axis magnetic field distribution (Gaussian fit to the measurement data is shown) of the ring magnet objective lens and simulated rays for beam energies of 25, 30, and 35 keV, giving a focal length of  $\sim 5.5$  mm at 30 keV.

### Point-projection measurements of the crossover and probe

Point-projection experiments were used to measure the electron beam crossover spot size (due to the focusing effect of the cathode cup) and probe size (due to the ring magnet objective lens). The schematic in figure 3b of the main text describes the experimental setup, where the source is either the beam crossover or the probe (depending on the experimental configuration employed), the object is a  $5\text{-}\mu\text{m}$ -width bar (from a metallic 2000 mesh), and the image is projected onto a phosphor screen. There are two scenarios in this schematic: one where the source is smaller than the width of the bar, and the other where it is larger. By measuring the umbra and penumbra of the resulting images, we can obtain the source size. Using geometry, the umbra and penumbra for the two scenarios outlined in figure 3b can be shown to be

$$(3) \quad d < b : \quad U = b + n(b-d)/z$$

$$P = nd/z$$

$$(4) \quad d > b : \quad U = b - n(d-b)/z$$

$$P = nd/z ,$$

where  $U$  is the width of the umbra,  $b$  is the width of the object,  $n$  is the distance from the object to the image,  $d$  is the width of the source,  $z$  is the distance from the source to the object, and  $P$  is the width of the penumbra. The distance between the source and the object is obtained based on the magnification seen in the images:

$$(5) \quad M = (z+n)/z ,$$

where  $M$  is the magnification. Since the projection images using the crossover as a source have a

slightly non-zero umbra width, we can assume that the crossover width is comparable to that of the mesh bar, so we can use equation (4) to calculate an upper bound of the source size that would result in an umbra equal to 0. This puts an upper bound of 6  $\mu\text{m}$  on the crossover diameter.

In the case of point-projection experiments using the probe formed by the objective lens as the source, the source diameter is much smaller than that of the mesh bar width given the small penumbra-to-umbra ratio seen in figure 3b of the main text. Using the system of equations (3) from above, we have two unknowns: the diameter of the source, and the distance from the source to the object. Taking the penumbra as the average of the two values gathered from the line plot in figure 3b (bottom row), along with the width of the umbra from the same figure, we find the distance from the source to the object to be 0.54 mm, and the diameter of the source to be 310 nm. Given that these calculations do not account for coulomb interactions in the electron beam, lensing effects from the mesh, or phosphor non-idealities, this measurement result is consistent with the above-calculated probe size of  $<250$  nm and, indeed, with our observed SEM imaging resolution.

### **Beam column**

The main body of the SEM consists of a 304 stainless steel pipe with a length of 30 cm and inner and outer diameters of 12.70 mm and 19.05 mm, respectively, welded to the bottom of the cathode compartment. The anode is an aluminum disc with a 1-mm spray aperture positioned at the top end of the column, 11.5 mm below the open end of the cathode cup, and is electrically connected to the rest of the column, which is grounded. A set of 4 small, 450-turn off-the-shelf electromagnets (with opposing pairs driven by the same current) enables transverse beam alignment (figure M3). Near the bottom of the column is a standard 100- $\mu\text{m}$ -diameter objective aperture (made of molybdenum). Immediately below the aperture reside two common off-the-shelf silicon pn-junction diodes which act as backscattered electron detectors. Their back sides (cathodes) are soldered onto a small printed circuit board, which is attached to the aperture holder disc and grounded, and their front sides (anodes) are soldered onto a wire that is brought out of the column through a small gap on the side; the gap is sealed around this feedthrough wire using low-vapour-pressure epoxy. Two sets of 4 electromagnets, identical to those used for alignment and wired for the appropriate arrangement of polarities, form the stigmators and scan coils, respectively (however, it should be noted again that the stigmators were not used for the images shown in figure 1 of the main text). The objective lens consists of two off-the-shelf, axially-magnetized neodymium ring magnets with inner and outer diameters of 19.05 mm and 31.75 mm, respectively, attached to one another in series, without any iron core. The use of permanent magnets to focus an electron beam has been studied extensively in the past<sup>20,21,90</sup>.

The bottom end of the column rests on the flat surface of an aluminum disc which holds the specimen, with an elastomer o-ring between the two (figure 2 of the main text). A small amount of vacuum grease is applied to the o-ring to enable the specimen holder disc to easily slide underneath the column while the system is under vacuum. This sliding movement, which is controlled by hand, forms the specimen movement mechanism. The instrument frame, which holds the column and houses the electronics, is made of aluminum.

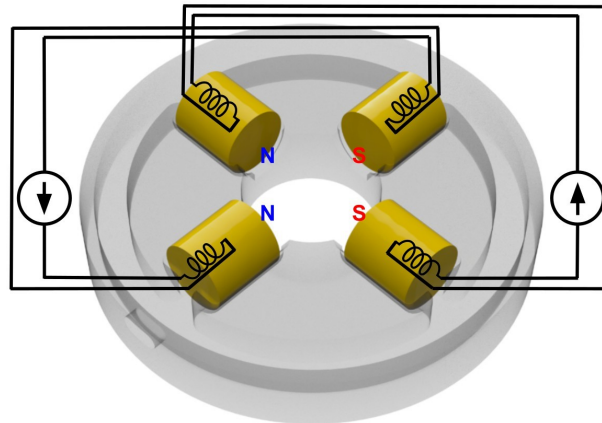


**Figure M3. Electromagnetic beam control.** The 4-electromagnet configuration wired for alignment and scanning functions. For the stigmator, the wiring is such that the same poles would be diagonally facing.

## Electronics

The electronics consist of drive circuitry for the laser, high-voltage supply, and electromagnets, and a transimpedance amplifier for the detectors. The scan driver control and detector signal acquisition are handled directly using a basic microcontroller, which communicates directly with the computer running the user interface. The laser beam, high-voltage supply, alignment coils, and detector are switched on and adjusted by manual switches and potentiometers mounted on the aluminum box housing the electronic circuits. The instrument is powered by a single 24 V AC-DC wall adapter, and uses less than 50 W of total power.

## Detailed design and components list

The detailed design of our prototype, including mechanical structure, electronic circuits, codes, and components list, will be provided separately online.

## Pumping system used for our prototype

Our prototype was pumped down using a turbomolecular pumping station through a port on the side of the cathode compartment. While the turbomolecular pump can produce ultra-high vacuum (UHV) in an appropriately sealed vacuum chamber, we did not use UHV or even high vacuum. In fact, our prototype is far from a UHV-compatible chamber: it uses a low-vacuum connection to the pump; an elastomer o-ring and vacuum grease loosely seal the specimen stage to the column allowing for relative movement; several other sealing points in the column and cathode compartment are made by manually applying epoxy; PCB parts and regular solder are used for mounting the detector within the column; and the system is routinely vented to atmosphere and pumped down without baking. Moreover, since the vacuum line is connected to the cathode compartment, the column is evacuated only through small openings, and the specimen compartment is evacuated through even narrower paths such as the objective aperture. These pose significant resistance to flow, hence the poor vacuum levels in the

cathode and specimen compartments as stated in the main text. In other words, such a turbomolecular pump is far more capable than needed by this SEM, but was a convenient option for our systematic experiments.

## **Acknowledgements**

We are grateful to R. Fabian Pease (Stanford University) for insightful discussions and consultations. We also thank Alex Anees for helping develop figures 1a and 2a and Gabriel Robinson-Leith for help with an early version of the software. We acknowledge funding from the Natural Sciences and Engineering Research Council of Canada (Grants No. RGPIN-2017-04608, RGPAS-2017-507958, I2IPJ538549-19, I2IPJ548806-20, RGPIN-2023-05154), the Canada Foundation for Innovation, and the British Columbia Knowledge Development Fund. This research was undertaken thanks in part to funding from the Canada First Research Excellence Fund, Quantum Materials and Future Technologies Program. We acknowledge CMC Microsystems for the provision of access to COMSOL Multiphysics®.

## **Author contributions**

AN conceived the microscope based on the Heat Trap photothermionic electron source. CK, AN, and AD carried out characterization experiments and designed, built, and operated the first prototype. AN and AD designed, built, and operated the second prototype. AN, CK, and AD wrote the manuscript. AN supervised the project.

## **Competing interests**

AN is a co-inventor on patents covering the content of this manuscript.

## **Correspondence**

Correspondence should be addressed to AN at [alireza.nojeh@ubc.ca](mailto:alireza.nojeh@ubc.ca).

## **Additional information**

Please see Supplementary Information and the figures S1-S7 therein.

## **Data availability**

The data that support the findings of this study are available within the paper and its Supplementary Information file. Detailed design documentation of the instrument will be provided separately online.

## **References**

1. Nojeh, A. Carbon nanotube photothermionics: toward laser-pointer-driven cathodes for simple free-electron devices and systems. *MRS Bulletin* **42**, 500–504 (2017).
2. Pease, R. F. W., Hayes, T. L., Camp, A. S. & Amer, N. M. Electron microscopy of living insects. *Science* **154**, 1185–1186 (1966). [*This is the scientific paper related to the San Francisco Chronicle article mentioned in the text.*]
3. Fly's tongue in 3-D – New microscope shows a remarkable sight, *Life Magazine* **56**(18), 69 (01 May 1964). [*Reporting on the work of R. R. Matta and colleagues at Westinghouse Electric Corporation.*]

4. Cybulski, J. S., Clements, J. & Prakash, M. Foldscope: origami-based paper microscope. *PLoS ONE* **9**, e98781 (2014).
5. Yanagisawa, H. *Quantum Kids Project* <https://hirofumiyanagisawa3.wixsite.com/quantum-kids-project>.
6. Everhart, T. E. Persistence pays off: Sir Charles Oatley and the scanning electron microscope. *Journal of Vacuum Science & Technology B* **14**, 3620–3624 (1996).
7. Delong, A. & Lencová, B. Early history of electron microscopy in Czechoslovakia. In *Advances in Imaging and Electron Physics* **220**, 127–152 (Elsevier, 2021).
8. Oatley, C. W. The early history of the scanning electron microscope. *Journal of Applied Physics* **53**, R1–R13 (1982).
9. Spreadbury, P. J. A simple scanning electron microscope. In *Advances in Imaging and Electron Physics* **133**, 153–158 (Elsevier, 2004).
10. Malac, M. *et al.* NanoMi: an open source (scanning) transmission electron microscope. *Microscopy and Microanalysis* **26**, 1810–1811 (2020).
11. Malac, M. *et al.* NanoMi open source (S)TEM platform: initial SEM implementation. *Microscopy and Microanalysis* **27**, 1062–1063 (2021).
12. Malac, M. *et al.* NanoMi: an open source electron microscope component integration. *Microscopy and Microanalysis* **28**, 3164–3165 (2022).
13. Malac, M. *et al.* NanoMi: an open source electron microscope hardware and software platform. *Micron* **163**, 103362 (2022).
14. Schreiber, M. *et al.* NanoMi: progress on an open-source electron microscope. *Microscopy and Microanalysis* **29**, 489–490 (2023).
15. NanoMi – ナノ美 An Open Source TEM, STEM and SEM Platform <https://sites.google.com/view/nanomi-org/home>.
16. Liu, W., Ambe, T. & Pease, R. F. Micro-objective lens with compact secondary electron detector for miniature low voltage electron beam systems. *Journal of Vacuum Science & Technology B* **14**, 3738–3741 (1996).
17. Honjo, I., Endo, Y. & Goto, S. Miniature electron beam column with a silicon micro field emitter. *Journal of Vacuum Science & Technology B* **15**, 2742–2748 (1997).
18. Crewe, D. A., Ruffin, M. M. & Feinerman, A. D. Initial images with a partially micromachined scanning electron microscope. *Journal of Vacuum Science & Technology B* **14**, 3808–3812 (1996).
19. Crewe, D. A. *A partially micromachined scanning electron microscope* PhD thesis (University of Illinois at Chicago, Chicago IL, USA, 1998).
20. Khursheed, A. Portable scanning electron microscope designs. *Journal of Electron Microscopy* **47**, 591–602 (1998).
21. Khursheed, A. Recent developments in scanning electron microscope design. In *Advances in Imaging and Electron Physics* **115**, 197–285 (Elsevier, 2001).
22. Khursheed, A., Nelliyan, K. & Ding, Y. Nanoscale imaging with a portable field emission scanning electron microscope. *Microelectronic Engineering* **83**, 762–766 (2006).

23. Winkler, D. *et al.* E. Experimental evaluation of a miniature electrostatic thin-foil electron optical column for high current and low-voltage operation. *Journal of Vacuum Science & Technology B* **16**, 3181–3184 (1998).
24. Bubeck, C.-D. *et al.* D. Miniature electrostatic lens for generation of a low-voltage high current electron probe. *Nuclear Instruments and Methods in Physics Research A* **427**, 104–108 (1999).
25. Lutsch, R.Y. & Plies, E. Initial resolution measurements of miniaturized electrostatic lenses for LVSEM. *Ultramicroscopy* **93**, 339–345 (2002).
26. Spallas, J. P., Silver, C. S., Muray, L. P., Wells, T. & El-Gomati, M. A manufacturable miniature electron beam column. *Microelectronic Engineering* **83**, 984–989 (2006).
27. Gaskin J. *et al.* Miniaturized scanning electron microscope for in situ planetary studies. In *Earth and Space 2010: Engineering, Science, Construction, and Operations in Challenging Environments* **2010**, 1246–1257 (ASCE, 2010).
28. Nelliyan, K. & Khursheed, A. Permanent magnet finger-size scanning electron microscope columns. *Nuclear Instruments and Methods in Physics Research A* **645**, 41–45 (2011).
29. Eastham, D. A. *et al.* A design for a subminiature, low energy scanning electron microscope with atomic resolution. *Journal of Applied Physics* **105**, 014702 (2009).
30. Sinno, I. *et al.* Fabrication of nanoscale electrostatic lenses. *Journal of Micromechanics and Microengineering* **20**, 095031 (2010).
31. Oh, T.-S., Kim, H.-S., Ahn, S. & Kim, D.-W. Design of an ultra-miniaturized electron optical microcolumn with sub-5 nm very high resolution. *Ultramicroscopy* **136**, 171–175 (2014).
32. Krielaart, M. A. R., Maas, D. J., Loginov, S. V. & Kruit, P. Miniature electron beam separator based on three stacked dipoles. *Journal of Applied Physics* **127**, 234904 (2020).
33. Chang, T. H. P., Kern, D. P. & Muray, L. P. Arrayed miniature electron beam columns for high throughput sub-100 nm lithography. *Journal of Vacuum Science & Technology B* **10**, 2743–2748 (1992).
34. Kratschmer, E. *et al.* An electron-beam microcolumn with improved resolution, beam current, and stability. *Journal of Vacuum Science & Technology B* **13**, 2498–2503 (1995).
35. Kruit, P. High throughput electron lithography with the multiple aperture pixel by pixel enhancement of resolution concept. *Journal of Vacuum Science & Technology B* **16**, 3177–3180 (1998).
36. Kruit, P. The role of MEMS in maskless lithography. *Microelectronic Engineering* **84**, 1027–1032 (2007).
37. Mohammadi-Gheidari, A. *196 beams in a scanning electron microscope* PhD thesis (Delft University of Technology, Delft, The Netherlands, 2013).
38. Mankos, M. *et al.* Optimization of microcolumn electron optics for high-current applications. *Journal of Vacuum Science & Technology B* **18**, 3057–3060 (2000).
39. Kim, H., Han, C., Kim, J., Kim, H. & Chun, K. Full MEMS monolithic microcolumn for wafer-level array. *Journal of Vacuum Science & Technology B* **22**, 2912–2916 (2004).
40. Weigand, H. *et al.* Microcolumn design for a large scan field and pixel number. *Journal of Vacuum Science & Technology B* **27**, 2542–2546 (2009).

41. Du, Z. *et al.* Design and fabrication of electrostatic microcolumn in multiple electron-beam lithography. In *Alternative Lithographic Technologies VIII* **9777**, 290–302 (SPIE, 2016).
42. Krysztof, M., Grzebyk, T., Górecka-Drzazga, A. & Dziuban, J. *A concept of fully integrated MEMS-type electron microscope*. 27<sup>th</sup> International Vacuum Nanoelectronics Conference (IVNC) (Engelberg, Switzerland, July 2014).
43. Białas, M., Grzebyk, T., Krysztof, M. & Górecka-Drzazga, A. Signal detection and imaging methods for MEMS electron microscope. *Ultramicroscopy* **244**, 113653 (2023).
44. Urbański, P., Szyszka, P., Białas, M. & Grzebyk, T. Point field emission electron source with a magnetically focused electron beam. *Ultramicroscopy* **258**, 113911 (2024).
45. Krasnow, B. *DIY scanning electron microscope - Overview* <https://benkrasnow.blogspot.com/2011/03/diy-scanning-electron-microscope.html> (2011).
46. Bazin, D. *et al.* Scanning electron microscopy—a powerful imaging technique for the clinician. *Comptes Rendus. Chimie* **25**, 37–60 (2022).
47. Yaghoobi, P., Moghaddam, M. V. & Nojeh, A. “Heat trap”: light-induced localized heating and thermionic electron emission from carbon nanotube arrays. *Solid State Communications* **151**, 1105–1108 (2011).
48. Vahdani Moghaddam, M., Yaghoobi, P. & Nojeh, A. Polarization-dependent light-induced thermionic electron emission from carbon nanotube arrays using a wide range of wavelengths. *Applied Physics Letters* **101**, 253110 (2012).
49. Yaghoobi, P., Vahdani Moghaddam, M. & Nojeh, A. Solar electron source and thermionic solar cell. *AIP Advances* **2**, 042139 (2012).
50. Vahdani Moghaddam, M., Yaghoobi, P., Sawatzky, G. A. & Nojeh, A. Photon-impenetrable, electron-permeable: the carbon nanotube forest as a medium for multiphoton thermal-photoemission. *ACS Nano* **9**, 4064–4069 (2015).
51. Mohammadbeigi, F., Whitehead, L., Divigalpitiya, R. & Nojeh, A. Observations of radiation-dominated rapid cooling of structures based on carbon nanotubes and graphene. *Advanced Engineering Materials* **22**, 1901315 (2020).
52. Chang, M., Fan, H. D. E., Chowdhury, M. M., Sawatzky, G. A. & Nojeh, A. Heat localization through reduced dimensionality. *Physical Review B* **98**, 155422 (2018).
53. Voon, K. J., Chang, M., Sawatzky, G. A. & Nojeh, A. Modeling energy exchange and heating within nanorod arrays due to near-field radiative coupling. *Journal of Applied Physics* **127**, 234302 (2020).
54. Bhardwaj, A., Phani, A. S., Nojeh, A. & Mukherji, D. Thermal transport in molecular forests. *ACS Nano* **15**, 1826–1832 (2021).
55. *Carbon nanotube and related field emitters: fundamentals and applications* (ed Saito, Y.) (John Wiley & Sons, 2010).
56. Yabushita, R., Hata, K., Sato, H. & Saito, Y. Development of compact field emission scanning electron microscope equipped with multiwalled carbon nanotube bundle cathode. *Journal of Vacuum Science & Technology B* **25**, 640–642 (2007).

57. Saito, Y. *et al.* Development of small sized FE-SEM equipped with a carbon nanotube field emitter. 29<sup>th</sup> International Vacuum Nanoelectronics Conference (IVNC) (Vancouver, BC, Canada, July 2016).
58. Kanth, S. K., Sharma, A., Park, B. C. & Kim, H. S. Multiwalled carbon nanotube field emitter as an electron source for a microcolumn. *Journal of Vacuum Science & Technology B* **34**, 011805 (2016).
59. Irita, M., Yamazaki, S., Nakahara, H. & Saito, Y. Development of a compact FE-SEM and X-ray microscope with a carbon nanotube electron source. *IOP Conference Series: Materials Science and Engineering* **304**, 012006 (2018).
60. Robinson, V. N. E. A wet stage modification to a scanning electron microscope. *Journal of Microscopy* **103**, 71–77 (1975).
61. Danilatos, G. D. Review and outline of environmental SEM at present. *Journal of Microscopy* **162**, 391–402 (1991).
62. Donald, A. M. The use of environmental scanning electron microscopy for imaging wet and insulating materials. *Nature Materials* **2**, 511–516 (2003).
63. Bogner, A., Jouneau, P.-H., Thollet, G., Basset, D. & Gauthier, C. A history of scanning electron microscopy developments: Towards “wet-STEM” imaging. *Micron* **38**, 390–401 (2007).
64. Dridi, K., Koshaman, A., Nojeh, A. & Sawatzky, G. Towards compact solar thermionic converters based on carbon nanotubes forests. 29<sup>th</sup> International Vacuum Nanoelectronics Conference (IVNC) (Vancouver, BC, Canada, July 2016).
65. Yuan, X. *et al.* A fully-sealed carbon-nanotube cold-cathode terahertz gyrotron. *Scientific Reports* **6**, 32936 (2016).
66. Han, J. S. *et al.* High-performance cold cathode X-ray tubes using a carbon nanotube field electron emitter. *ACS Nano* **16**, 10231–10241 (2022).
67. Green, E. D. & Kino, G. S. Atmospheric scanning electron microscopy using silicon nitride thin film windows. *Journal of Vacuum Science & Technology B* **9**, 1557–1558 (1991).
68. Nishiyama, H. *et al.* Atmospheric scanning electron microscope observes cells and tissues in open medium through silicon nitride film. *Journal of Structural Biology* **169**, 438–449 (2010).
69. Nguyen, K. X., Holtz, M. E., Richmond-Decker, J. & Muller, D. A. Spatial resolution in scanning electron microscopy and scanning transmission electron microscopy without a specimen vacuum chamber. *Microscopy and Microanalysis* **22**, 754–767 (2016).
70. Kang, D. J. *et al.* Atmospheric scanning electron microscopy and its applications for biological specimens. *Microscopy Research and Technique* **82**, 53–60 (2019).
71. Cremer, J. *et al.* Atomic-scale electron microscopy at ambient pressure. *Ultramicroscopy* **108**, 993–998 (2008).
72. Ominami, Y., Nakahira, K., Kawanishi, S., Ushiki, T. & Ito, S. A novel approach for scanning electron microscopic observation in atmospheric pressure. SPIE Scanning Microscopies (Monterey, California, United States, Sept. 2014).
73. Ominami, Y., Kawanishi, S., Ushiki, T. & Ito, S. A novel approach to scanning electron microscopy at ambient atmospheric pressure. *Microscopy* **64**, 97–104 (2015).
74. Han, Y., Nguyen, K. X., Ogawa, Y., Park, J. & Muller, D. A. Atomically thin graphene windows that enable high contrast electron microscopy without a specimen vacuum chamber. *Nano Letters* **16**,

7427–7432 (2016).

75. Meredith, P., Donald, A. M. & Thiel, B. Electron-gas interactions in the environmental scanning electron microscope gaseous detector. *Scanning* **18**, 467–473 (1996).

76. Zotta, M. D., Nevins, M. C., Hailstone, R. K. & Lifshin, E. The determination and application of the point spread function in the scanning electron microscope. *Microscopy and Microanalysis* **24**, 396–405 (2018).

77. Nevins, M. C. *Point spread function determination in the scanning electron microscope and its application in restoring images acquired at low voltage* PhD thesis (Rochester Institute of Technology, Rochester NY, USA, 2019).

78. Hagita, K., Higuchi, T. & Jinnai, H. Super-resolution for asymmetric resolution of FIB-SEM 3D imaging using AI with deep learning. *Scientific Reports* **8**, 5877 (2018).

79. Wang, C., Ding, G., Liu, Y. & Xin, H. L. 0.7 Å resolution electron tomography enabled by deep-learning-aided information recovery. *Advanced Intelligent Systems* **2**, 2000152 (2020).

80. Clusiau, S., Piché, N., Provencher, B., Strauss, M. & Gauvin, R. Automated SEM acquisitions and segmentation with AI. *Microscopy and Microanalysis* **29**, 458–459 (2023).

81. Leitherer, A., Yeo, B. C., Liebscher, C. H. & Ghiringhelli, L. M. Automatic identification of crystal structures and interfaces via artificial-intelligence based electron microscopy. *npj Computational Materials* **9**, 179 (2023).

82. Crozier, P. A. *et al.* The impact of artificial intelligence on *in situ* electron microscopy. *Microscopy and Microanalysis* **29**, 1595–1596 (2023).

83. Kalinin, S. V. *et al.* Machine learning for automated experimentation in scanning transmission electron microscopy. *npj Computational Materials* **9**, 227 (2023).

84. Chowdhury, M. M., Young, J. F., Sawatzky, G. A. & Nojeh, A. *Broadband infrared hyperspectroscopy with high spatial resolution for the study of nanoscale thermal emitters in vacuum*. 36<sup>th</sup> International Vacuum Nanoelectronics Conference (IVNC) (Cambridge, MA, USA, July 2023).

85. Kuzyk, C. T. *Low-cost scanning electron microscope* MASc Thesis (University of British Columbia, Vancouver BC, Canada, 2020).

86. Han, C., Sul, I. & Cho, B. Edge shadow projection method for measuring the brightness of electron guns. *Review of Scientific Instruments* **88**, 023302 (2017).

87. Cheng, K. *et al.* Fabrication and simulation of self-focusing field emission X-ray tubes. *Applied Sciences* **5**, 942–954 (2015).

88. Chang, M., Sawatzky, G. A. & Nojeh, A. *Experimental investigation of the energy distribution of thermionic electrons*. 35<sup>th</sup> International Vacuum Nanoelectronics Conference (IVNC) (Seoul, South Korea, July 2022).

89. Chang, M. *Energy distribution of thermal electron emission* PhD thesis (University of British Columbia, Vancouver BC, Canada, 2024).

90. Adamec, P., DeLong, A. & Lencová, B. Miniature magnetic electron lenses with permanent magnets. *Journal of Microscopy* **179**, 129–132 (1995).

**SUPPLEMENTARY INFORMATION for**  
**Concept and Demonstration of a Low-cost Compact Electron Microscope**  
**Enabled by a Photothermionic Carbon Nanotube Cathode**

Casimir Kuzyk, Alexander Dimitrakopoulos, Alireza Nojeh\*

Department of Electrical and Computer Engineering, The University of British Columbia, Vancouver BC, V6T 1Z4, Canada

Quantum Matter Institute, The University of British Columbia, Vancouver BC, V6T 1Z4, Canada

\*Corresponding author: [alireza.nojeh@ubc.ca](mailto:alireza.nojeh@ubc.ca)

### **Carbon nanotube forest growth and characterization**

The carbon nanotube (CNT) forests were grown in-house by chemical vapour deposition (CVD). A low-resistivity (0.001-0.005  $\Omega\cdot\text{cm}$ ) Si wafer was used as the growth substrate. 10 nm of  $\text{Al}_2\text{O}_3$  and 1 nm of Fe were deposited on the substrate using thermal evaporation. The coated wafer was diced into  $\sim 5 \times 5$  mm<sup>2</sup> squares before being placed in the CVD reaction vessel. The vessel was first purged with argon before ramping up the temperature to 750 °C for the annealing stage, where a flow of argon and hydrogen gas enables the formation of small iron islands that act as catalysts for nanotube growth. Next, the high temperature was maintained while a flow of ethylene gas was introduced, which decomposes to form the multi-walled CNTs. This is a well-established procedure and has been used extensively to grow CNT forests of millimeter heights—more detail can be found in [S1].

### **Vacuum system**

#### *Specimen flexibility*

To further illustrate how the demonstrated SEM platform adapts to the user, we present a series of images that highlight the user-friendliness of the system and its tolerance to various specimen conditions. In figure S1 we compare images of cardboard with a sputtered metal coating, with no coating, and after being submerged in water directly before imaging. It should be noted that images of fair quality were still obtained with the uncoated, non-conductive cardboard specimen, despite some charging artifacts. Of particular interest is the wet specimen, as the sample preparation was extremely simple and accessible, yet it displayed a significant image quality improvement compared to the uncoated specimen. Once the small wet cardboard specimen is introduced into the low vacuum sample chamber, presumably most of the water rapidly evaporates, but it appears to leave behind a conductive residue on the specimen, resulting in improved image quality.

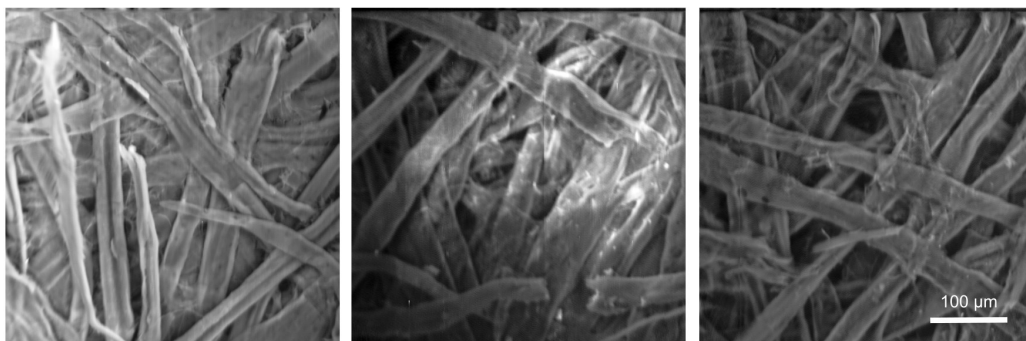


**Figure S1. Effect of coating on imaging of insulating specimen.** Comparison of (left) metal coated, (middle) uncoated, and (right) wet cardboard.

The images shown in figure S2 are of a fresh maple leaf that was harvested outside of our laboratory mere minutes before imaging. Other than cutting the specimen to an appropriate size for the sample chamber, no processing was necessary. Similar to the wet cardboard specimen, charging artifacts were negligible in these images. The ease with which specimens can be imaged in this microscope is comparable to an optical microscope; however, in addition to higher image quality (notably due to the much higher depth of focus), the SEM has the advantage of being able to image specimens with significant height variations at high magnification, whereas with an optical microscope there is a risk of striking the objective lens.

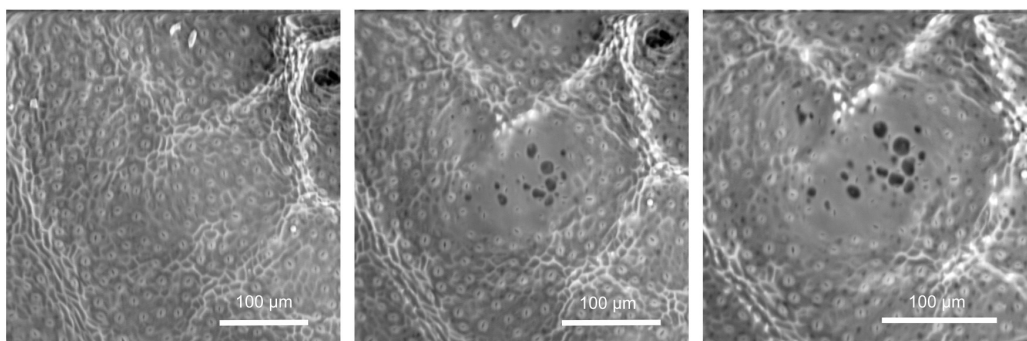


**Figure S2. Imaging of biological specimen without any sample preparation.** Fresh maple leaf harvested only minutes before imaging. The progression from left to right shows damage to the sample over the course of 10 minutes from exposure to the electron beam, particularly in the middle of the sample where the exposure was increased when zooming in.

### *Pumpless/sealed-off operation*

As discussed in the main text, an ultimate goal would be to develop a pumpless system. As a proof of concept, we inserted a soft copper connection in the vacuum line, pumped the instrument down, baked

it at  $<100$  °C for several hours, and pinched-off the copper connection. For this particular test, a tin-sphere-on-carbon calibration standard had been placed within the end of the column, and we were able to image it without any problem even at an electron beam energy of 30 keV. This sealed-off system maintained vacuum for only about an hour, but this is due to the rough nature of the various seals on this prototype and the minimal cleaning and bake-out employed in this experiment. For constructing a permanent device, well-established manufacturing technologies of cathode ray tube television sets are perfectly adequate. Modern examples involving carbon nanotube electron emitters are reported in [S2, S3].

For a practical pumpless instrument, as discussed in the main text, an electron-transparent window must be included at the end of the column to allow the electrons to exit and strike the specimen in its natural environment. We have experimented with silicon nitride membranes of various thicknesses as the window. A wider window facilitates electronic scanning of a wider area on the specimen, and we have observed that 50-nm-thick membranes as wide as 500  $\mu\text{m}$  can withstand the requisite 1-atmosphere pressure differential. The effect of electron scattering in rough vacuum on imaging is shown in figure S3. The effect of electron scattering in the silicon nitride membrane is also shown in figure S3, where there is a decrease in contrast due to the increased background noise from the scattered electrons, as discussed in the main text.

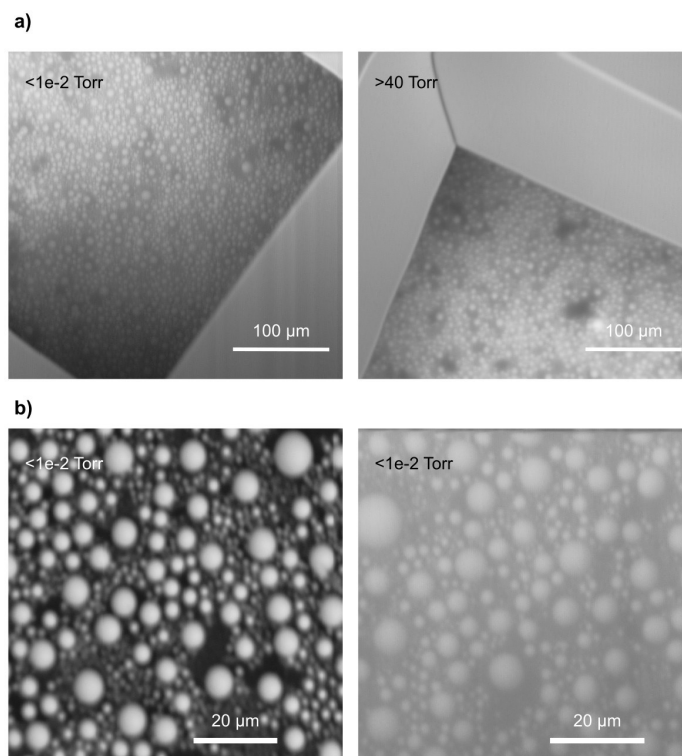


**Figure S3. Effect of electron-transparent membrane and vacuum level.** a) Tin-on-carbon calibration standard imaged in (left) vacuum and (right)  $>40$  Torr. In both cases, a 50-nm-thick silicon nitride membrane separated the electron column from the specimen. The large rectangular structure seen in the images is the silicon frame of the nitride membrane. b) Tin-on-carbon calibration standard imaged (left) directly and (right) through a 50-nm-thick silicon nitride membrane. The

instrument's contrast and brightness settings were kept the same for both images.

## Electron-optical system

### Objective lens

The ring magnets we used for the objective lens were stock components, and thus not manufactured with high tolerances; they even had visible defects, leading to aberrations such as astigmatism. Smaller-diameter ring magnets are expected to have less circular distortion; they also provide a more concentrated magnetic field and thus a smaller focal length and better focusing. However, smaller-diameter magnets impose size limitations on the sample, especially if the focal plane is within the bore of the lens. It should also be noted that demagnetization was observed when the lens was subject to electron beam radiation, making it impractical to place smaller-diameter lenses within the column itself. An imaging performance comparison among ring magnets with different sizes is shown in figure S4. The key take-away is that the instrument can operate well with a wide range of magnets—the exact choice depends on the builder's preference and use case.

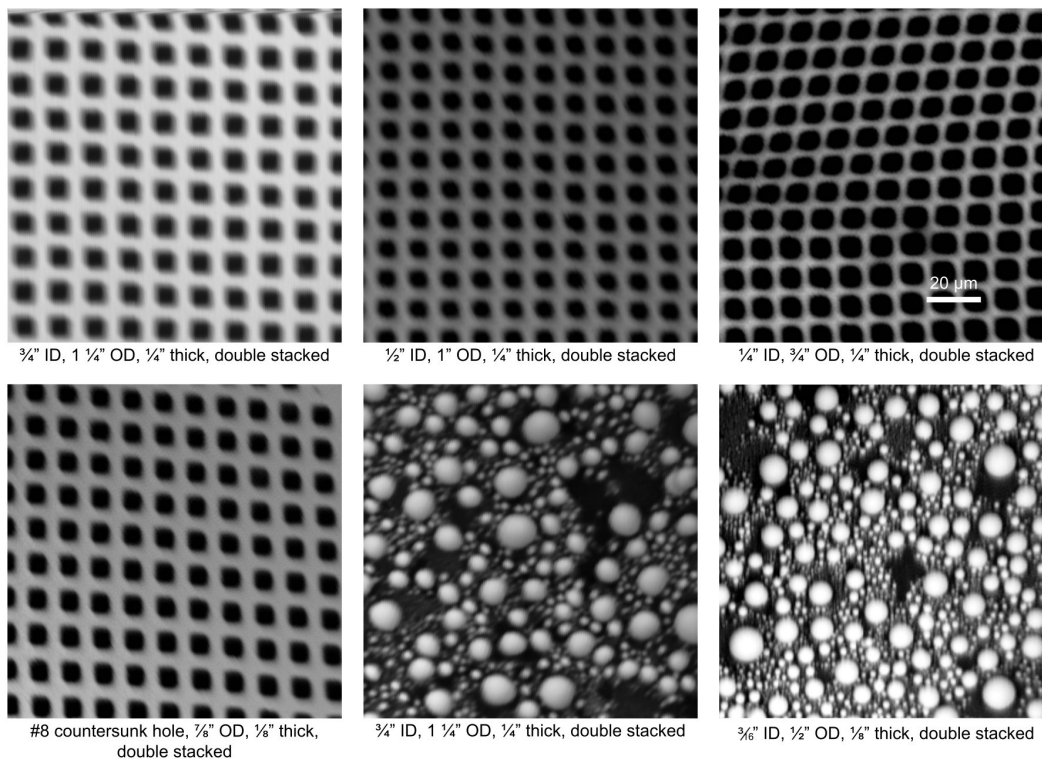


**Figure S4. Flexibility of choice of permanent magnet for the objective lens.** Imaging comparison using different sizes of neodymium ring magnets. The first 4 images are of a metallic 2000 mesh, and the remaining 2 images are of a tin-on-carbon calibration standard.

### *Electron-optics improvements*

A number of future improvements to the electron-optical system can be envisioned. Better focusing of the excitation laser and thus a more confined Heat Trap spot on the CNT forest surface would lead to a smaller emission area, and thus a smaller probe size and higher resolution. By using a beam expander and a focusing lens with a smaller focal length, one could decrease the size of the Heat Trap commensurately. This, however, would require better mechanical precision to position the laser focal spot at the surface of the CNT forest, given the decreased depth of focus. The resolution could also be improved by adding a condenser lens, either by creating a magnetic circuit from the secondary field of the existing objective lens, or in the form of an additional ring magnet placed further up the beam column. This would decrease the total probe current, and may require further improvements to the electron detector and amplifier system to utilize the weaker signal. We expect that these improvements would allow the electron probe size to be reduced to  $\sim 50$  nm.

While we did not use a stigmator for the images presented in the main text, we have observed a significant improvement in image quality when using a stigmator, as shown in figure S5.



**Figure S5. Effect of stigmation.** Imaging comparison of an array of rectangles on a silicon wafer with (left) the stigmator off and (right) the stigmator on. Sample provided by Lumiense Photonics Inc.

### **Electromagnetic noise and shielding**

A primary source of noise present in the images generated by the current prototypes is 60 Hz environmental noise. In order to study the impact of low-frequency magnetic field noise on the electron beam, an aluminum shield lined with a thin layer of mu-metal was used. Examples of imaging with and without the shield are shown in figure S6. The power circuitry for the electromagnets is designed with high power supply rejection ratios, to minimize the effect of noise from the device itself. It should be noted that the images shown in the main text are taken without the mu-metal shielding.

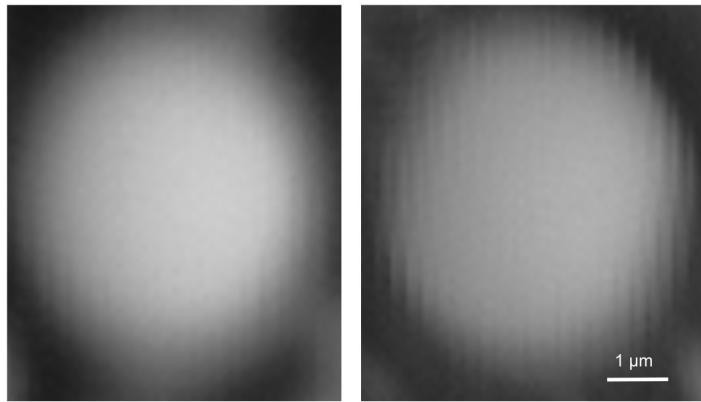


**Figure S6. Effect of electromagnetic noise.** Imaging comparison of a  $\sim 5\text{-}\mu\text{m}$ -diameter tin sphere with (left) and without (right) the mu-metal shielding. 60 Hz environmental noise appears as periodic, nearly vertical stripes with the chosen image scan frequency.

### **Laser, high-voltage, and X-ray safety**

An opaque shield covers the laser and electron source assembly to prevent stray laser reflections. The high-voltage lead of the power supply is covered by a thick layer of high-voltage insulating putty, which is surrounded by a grounded metallic cylinder, before entering the vacuum chamber using a ceramic-insulated feedthrough rated to 50 kV. X-ray generation by the high-energy electrons is expected to be minimal since the emission current is of the order of only a few microamperes, but precautions are nonetheless necessary. The main areas of X-ray generation are expected to be at the anode plate, objective aperture, and specimen, which are collectively struck by the majority of the electrons. The design of the instrument is such that X-rays would be significantly attenuated by the stainless steel beam column and the housing. During experiments we used a radiologist's X-ray sensor to monitor any possible stray dose and recorded doses were always significantly below allowed safe limits. Appropriate safety measures must be taken for different embodiments of the instrument.

### **Additional micrographs**

We have imaged a wide variety of specimens with our two prototypes, from biological curiosities to novel engineered materials. Figure S7 gives more examples of images that were taken with this instrument.

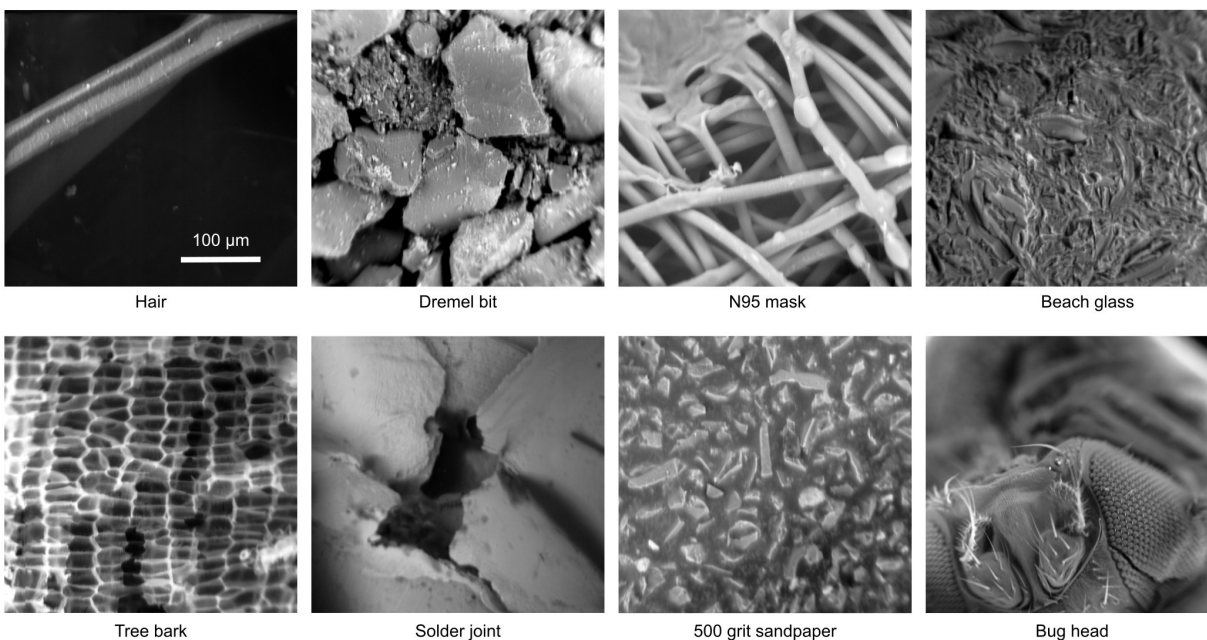


**Figure S7. Various specimen images.** A selection of additional micrographs obtained using this SEM, which highlight its broad range of applicability (scale bar approximate).

## References

- S1. Voon, K. *Modelling contributing factors to heat trapping in carbon nanotube forests* PhD thesis (University of British Columbia, Vancouver BC, Canada, 2021).
- S2. Yuan, X. *et al.* A fully-sealed carbon-nanotube cold-cathode terahertz gyrotron. *Scientific Reports* **6**, 32936 (2016).
- S3. Han, J. S. *et al.* High-performance cold cathode X-ray tubes using a carbon nanotube field electron emitter. *ACS Nano* **16**, 10231–10241 (2022).